Invited Article

(INVITED) Determination of non-linear refractive index of laser crystals and ceramics via different optical techniques

Laurent Lamaignère [a,*], Guido Toci [b,c], Barbara Patrizi [b,c], Matteo Vannini [b,c], Angela Pirri [d], Samuele Fanetti [c,e], Roberto Bini [c,e,f], Gabriel Mennerat [g], Andrius Melninkaitis [h], Luise Lukas [i], Joachim Hein [i]

[a] CEA-CESTA, F33116 Le Barp, France
[b] National Institute of Optics, National Research Council ,INO-CNR, Via Madonna Del Piano, 10 50019, Sesto Fiorentino (Florence), Italy
[c] European Laboratory for Non-Linear Spectroscopy (LENS), Via Nello Carrara 1, 50019, Sesto Fiorentino (Florence), Italy
[d] Institute of Applied Physics "N. Carrara", National Research Council, IFAC-CNR Via Madonna Del Piano 10 50019 Sesto Fiorentino (Florence), Italy
[e] Institute of Chemistry of the Organometallic Compounds, National Research Council, ICCOM-CNR, Via Madonna Del Piano 10, 50019, Sesto Fiorentino (Florence), Italy
[f] Department of Chemistry "Ugo Schiff", University of Florence, Via Della Lastruccia, 3,50019, Sesto Fiorentino, (Florence), Italy
[g] CEA, Iramis, SPAM, Saclay, France
[h] Laser Research Center, Vilnius University, Sauletekio ave. 10, LT, 10223, Vilnius, Lithuania
[i] Institute of Optics and Quantum Electronics, Friedrich-Schiller-University Jena and Helmholtz Institute, Jena, Germany

ARTICLE INFO

ABSTRACT

The exact knowledge of optical material parameters is crucial for laser systems design. Therefore, the work reported herein was dedicated to the determination of an important parameter that is typically not known or only known with insufficient precision: the Kerr coefficient determined by the third order non-linearity, also called the n_2-parameter. The optical Kerr effect is responsible for the accumulated nonlinear phase (the B-integral) in high energy laser amplifiers, which often represents a serious limitation. Therefore, the knowledge of n_2 is especially required for new types of laser materials. In this paper we report measurements carried out on the widely used optical material Ytterbium-doped Yttrium Aluminium Garnet (Yb:YAG) ceramics. Furthermore, the new Neodymium-doped Calcium Fluoride (Nd:CaF$_2$) crystal was investigated. Specifically, three different approaches have been employed to determine experimentally the nonlinear refractive index of these materials. Thus classical Z-scan technique (at two different wavelengths), the degenerated four waves mixing and the time-resolved digital holography techniques, were compared. These different approaches have permitted the precise measurements of these parameters as well as their dispersion estimations.

1. Introduction

Laser amplifiers capable of producing energetic nanosecond pulses are one of the main tools for ultra-high intensity laser-matter interaction research and high-energy applications such as particle acceleration [1], intense X-ray generation [2], inertial confinement fusion [3] and plasma acceleration [4,5]. Proof of principle demonstrations have so far been performed using facilities relying on flash-lamp pumped systems, which are limited in terms of pulse repetition-rates and efficiencies [6]. An innovative approach, based on Diode-Pumped Solid-State Laser (DPSSL) technology allows overcoming these limitations as it enables multi-J

pulse energy production at multi-Hz repetition rate operation [7–9]. To that purpose, Yb^{3+}-doped Yttrium Aluminum Garnet (Yb:YAG) is one of the most efficient materials for high-energy, high-repetition rate DPSSL systems [10]. Another new suitable solid state laser material is Nd:CaF$_2$ [11,12]. CaF$_2$ is well known as a host for Yb^{3+} ions as an efficient laser medium [13,14], which analogously to the Yb:YAG counterpart can be pumped by laser diodes.

Advantages to use doped CaF$_2$ as the active laser medium are the typically long fluorescence lifetime of the rare earth ions, what is especially important for diode pumped lasers systems, and the low linear as well as nonlinear refractive index of fluorides. This is why this host

may be an alternative to the long-known YAG. Since emission bands of Yb:CaF$_2$ are very broad and the fluorescence lifetime is long, the cross sections become low and efficient energy extraction from amplifiers is challenging [15]. Even high intensities with ultra-short pulses as short as 100 fs [16] can be generated with this material, high energy densities are required, that increase the probability of laser damage in the active medium itself. In contrast, Nd-doped hosts exhibit typically higher cross sections and therefore Nd:CaF$_2$ and Yb:YAG are among the most promising materials for modern diode pumped lasers. The induced changes in the refractive index are linearly proportional to light intensity and a non-linear part of the refraction is described by the nonlinear refractive index n_2, that is related to the real part of the third order nonlinearity. The third order nonlinearity is the reason for the onset of filamentation of the beam in an amplifier due to self-focusing. It plays also an important role in optical damage. In order to avoid such effects, the so called B-integral [17], that is the accumulated nonlinear phase, has to be kept at a low level in the whole laser chain. Therefore, the knowledge of this parameter and its measurement capability are of very high importance for the design of the laser. The lower is the nonlinearity the higher the fluence in the amplifier which can be tolerated. This is a prerequisite for high extraction efficiency in case of energetic ns-pulses as well as for fs-pulses through the chirped pulse amplification (CPA) scheme. In the latter case the B-integral in amplifiers is also responsible for the pre-pulse generation through the interaction of the main pulse with post-pulses [18]. In order to include all these effects in laser design the exact knowledge of the nonlinear refractive index is necessary, and its comparison for the promising laser materials Nd:CaF$_2$ and Yb:YAG is worth to be reported.

For the accurate measurement of the n_2, setups and procedures with improved accuracy have been developed and used for material investigations: the well-known Z-scan technique [19–23], the degenerate-four-wave-mixing (DFWM) [24,25] and the time-resolved digital holography (TRDH) [26]. Since these techniques can be very error prone, due to the lack of an exact knowledge of the light intensity distribution in time as well as in space, the comparison with a standard material, for which the n_2 is known with high precision, is typically made. This allows a deduction of the n_2-value including all secondary effects related to the nonlinear refractive index in the material.

The paper is organized as follows. The two materials are introduced in Section 2, while in Section 3 the four partner's experimental set-ups and the techniques developed and used for nonlinear refractive index measurements are described; finally, in Section 4, experimental results which allowed us to discuss the dispersion and the accuracy of the measurements are reported.

2. Materials

2.1. Nd:CaF$_2$ crystals

Neodymium doped calcium fluoride was investigated because of its very broad absorption and emission bands, which are comparable in width to those of glasses currently employed in high-energy lasers. The high thermal conductivity of Nd^{3+}:CaF$_2$ [27] allows it to withstand a great amount of thermal load, thus making it suitable for high-energy pulsed laser amplifiers. Nd^{3+} doped CaF$_2$ offers attractive spectroscopic glass-like features while still being single crystals having thus a high thermal conductivity which makes this material suitable for applications such as high-energy pulsed laser amplifiers and particularly appealing for amplifiers in new generation of laser fusion facilities [12]. In this study, samples of CaF$_2$:0.5%Nd, *X*%Lu (with *X* ranging from 0 to 20%) prepared by the Bridgman growth technique were investigated. Indeed, codoping Nd:CaF$_2$ single crystals with Lu^{3+} non optically active ions significantly improves their absorption, emission, and fluorescence lifetime properties and their laser performance. An increase in Lu^{3+} concentration tends to increase the Nd^{3+} transitions' quantum efficiency, as a consequence of the replacement of Nd–Nd clusters by Nd–Lu

clusters. Spectroscopic measurements were performed that permitted to identify the individual absorption and emission cross-section spectra of the main Nd^{3+} emitting centres, along with their fluorescence and radiative lifetimes [12,28]. Samples, labeled A and B below, were 5 mm × 5 mm x 5 mm and sample C was 3 mm thick. All the facets were also optically polished in order to allow measurements in probe-pump configurations with orthogonal beams.

2.2. Yb:YAG ceramics

Yb^{3+}-doped Yttrium Aluminum Garnet is one of the most efficient materials for high-energy, high-repetition rate DPSSL systems. Indeed, Yb^{3+} is an active laser ion which offers long fluorescence lifetimes, reasonable gain cross section, and low quantum defect, with efficient and reliable high power laser diodes at its pump wavelength. YAG as the host medium offers good thermo-mechanical and thermo-optical properties. Substrates used for the experimental measurements consisted of 2 at-% doped polycrystalline Yb:YAG [29] and the maximum doping gradient over the samples was expected to be 0.015 at-%. Their dimensions were 25 mm × 25 mm × 5 mm, and the facets were polished to rms (root-mean square) surface roughness values below 0.5 nm. Transmitted wavefront measurements were performed over a 22 mm × 22 mm area (about 92% of the optics aperture) using a Zygo xpD interferometer and analysed using Zygo Mx software. Over the measurement window, the rms wavefront error was 0.01 λ and the peak-to-valley wavefront value was 0.085 λ for 1030 nm light and for a single pass through the sample. Their Young's modulus was about 297±4 GPa.

3. Experimental set-ups and procedures

Nonlinear refractive index (n_2) measurements with improved accuracy have been developed by four different partners by means of three different techniques reported as following:

- Set-up A: **Z-scan** procedure at 800 nm/50 fs - 200ps. This setup was qualified with common isotropic materials and centro-symmetric crystals in the femtosecond regime.
- Set-up B: **Z-scan** procedure at 1064 nm/30 ps.
- Set-up C: Degenerate-four-wave-mixing (**DFWM**) technique with temporal resolution at 800 nm/60 fs and 1030 nm/150 fs.
- Set-up D: Time-resolved digital holography (**TRDH**) technique pumped at 1030 nm & 515 nm/300 fs and tested by 530 nm (tunable)/25 fs.

3.1. Z-scan schemes @ 800 nm and @ 1064 nm

This single beam standard technique for the measurement of the nonlinear refractive index and nonlinear absorption of optical materials is based on the measurement of the self-focusing effect of a laser beam, induced by a nonlinear sample, which is moved along the propagation direction (Z axis). The self-focusing effect affects the propagation of the beam and its spatial structure in the far field. Knowledge of the spatial characteristics of the probe beam is mandatory in order to obtain a quantitative assessment of the nonlinear parameters.

A first set-up based on the Z-scan has been developed to measure the nonlinear refractive index coefficient n_2 of optical materials at 800 nm (see Fig. 1). The facility is based on a Ti:sapphire laser equipped with a number of frequency-conversion stages (OPA, SFG, DFG). It delivers femtosecond pulses over a broad spectral range, from the UV (266 nm) to the mid-infrared (2000 nm). The experimental station is equipped with its own compressor which makes it possible to set independently the pulse durations. Quartz and un-doped sapphire samples were used to calibrate the bench.

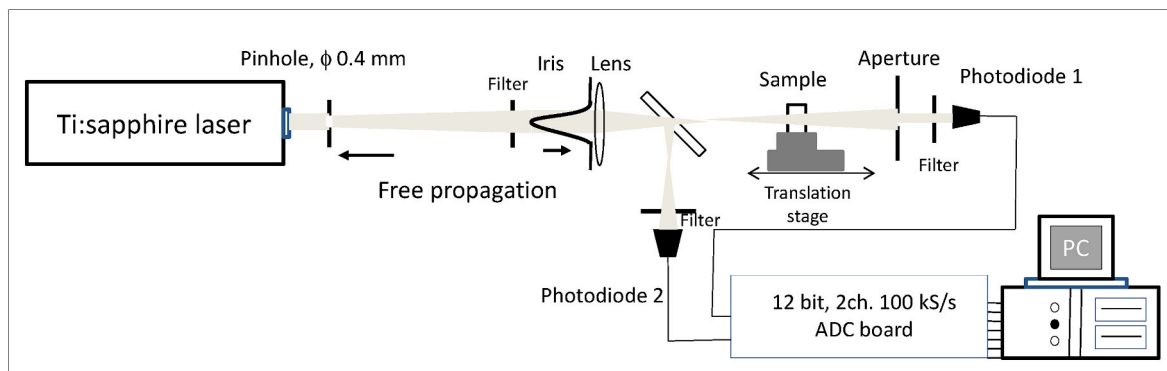Miro simulations [30] based on the measured spatio-temporal

Fig. 1. Z-scan experimental set-up [21]. Pulse duration control using a home-made SPIDER (Spectral Phase Interferometry for Direct Electric Field Reconstruction).

characteristics of the input beam were used to calibrate the bench on two well-known materials: fused-silica and sapphire (Fig. 2). This setup once qualified with common isotropic materials and centrosymmetric crystals in the femtosecond regime was used to measure nonlinear index of Nd:CaF$_2$ crystals and Yb:YAG ceramics.

Another bench based also on the Z-scan technique [19] was used. In this case, the so-called trimmed Airy beam was used, as it provides higher sensitivity and it is easier to realize than a conventional ideal Gaussian beam [20]. The trimmed Airy beam structure has been obtained by selecting a portion of the laser beam with a small pinhole, and letting it propagate for a distance of about 5 m, so that the beam intensity distribution assumes the shape of an Airy diffraction pattern. An iris selects the central lobe of the beam which is sent to the experiment (Fig. 1). The maximum pulse energy used in the experiment was about 100 μJ on the sample. The experimental set up is based on a 10 Hz oscillator/amplifier Nd:YAG laser (EKSPLA), with harmonic generation, with a pulse duration in the range 20–40 ps.

The probe beam sent to the sample has an overall energy of several tens of μJ, and it is focused on a minimum diameter of some tens of μm, resulting in an overall peak intensity in the range of 10^2 GW/cm^2. The sample is placed on a motorized translation stage with a resolution of 2 μm, and an overall translation length of 50 mm. The incident pulse is sampled by a beam splitter which sends part of the pulse energy to a reference detector which monitors the incident pulse energy; the pulse is then attenuated by a variable filter and focused on the sample by a spherical lens. After the focusing, the beam propagates for a distance much longer than the Rayleigh distance and impinges on a small aperture. The transmitted energy is measured by a silicon photodiode, whereas a beam splitter placed before the lens sends part of the pulse energy to a second photodiode, used as a reference. An analog to digital conversion (ADC) board simultaneously acquires the two signals, which are then stored and processed on a PC. In the usual measurement protocols, the Z-scan traces on a given sample are acquired at various input

pulse energies, modulated by variable attenuators. The overall sensitivity in the transmission variation thus achieved is around 1% for the samples with good optical quality.

For each position of the variable attenuator, the pulse energy incident on the sample is measured before and after each measurement run by a pyroelectric laser energy meter (Laser Precision RJ 735). The reference and the measurement detectors are two large area silicon photodiodes equipped with a double stage integrator/amplifier (internally designed and built). The signals from the detectors are acquired by a 16 bit, 20 Ksamples/sec sampling board. For each sample position, the incident pulse energy and the on axis energy are acquired for several laser pulses (typically 50); for each individual pulse the transmission of the pinhole is calculated and then averaged over the pulses set; pulses with energy higher than or lower than 3% of the average value are discarded.

The laser pulse duration has been measured by means of second order autocorrelation in a frequency doubling crystal. The spatial intensity distribution in the lens focus has been acquired by a silicon CCD camera, with a spatial resolution (pixel pitch) of 6.45 μm. The Figs. 3 and 4 below show the pulse autocorrelation trace and the beam profile in the focus.

Data analysis is based on numerical models [20], as it will be detailed below. The whole set-up is calibrated using samples made of amorphous SiO$_2$ whose n_2 coefficient is well known. The fused silica sample used as standard had a length of 6.15 mm. Differences in the sample optical thicknesses are accounted for by means of the numerical models mentioned above.

For each sample, several z-scan runs were carried out at different levels of incident energy E, adjusted with the variable attenuator (see Fig. 5). A further run at the lowest possible incident energy level was also acquired and used to subtract the fluctuations in the sample transmission due to small internal or surface defects, irregularities and so on. The results of a typical series of measurements at different values
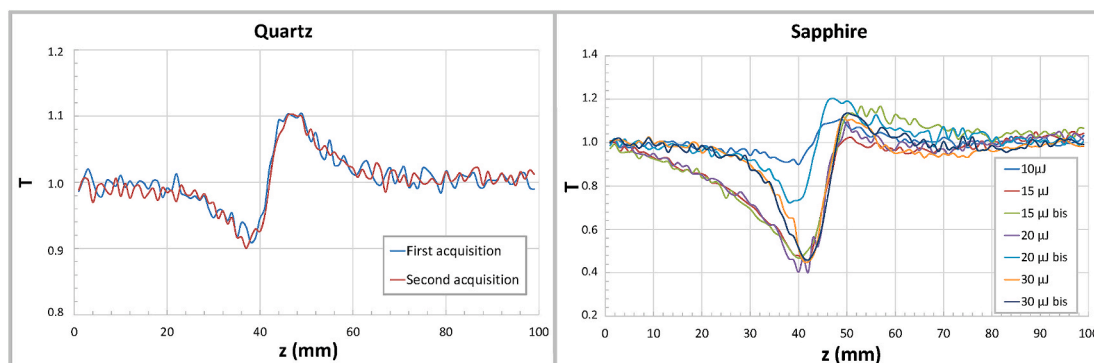

Fig. 2. Calibration of the Z-scan measurements using quartz (left) and sapphire (right, repeatability at different energy levels) samples.
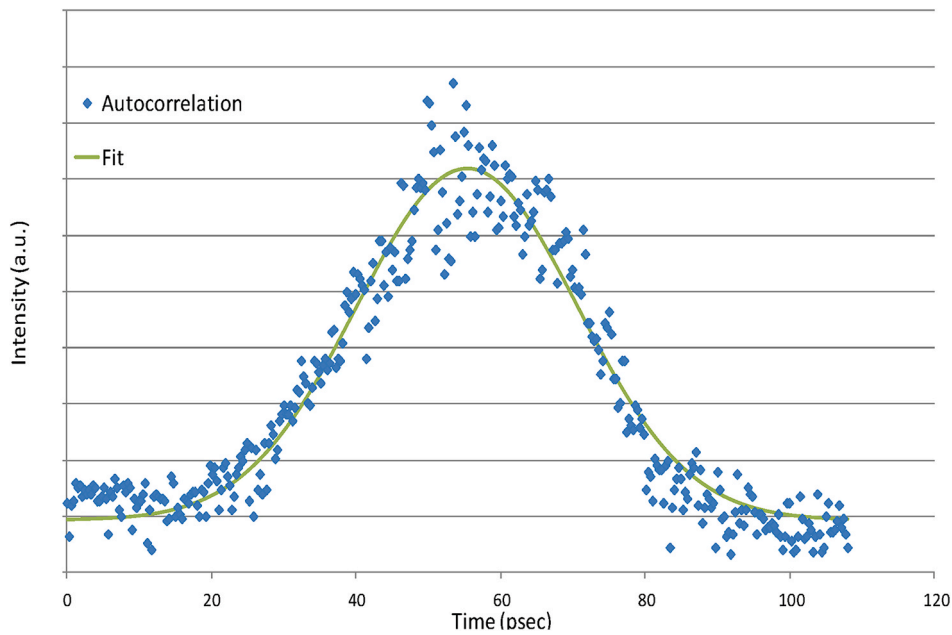
Fig. 3. Second order autocorrelation trace of the laser pulse used in the experiments. The calculated pulse duration is 27 psec (FWHM).
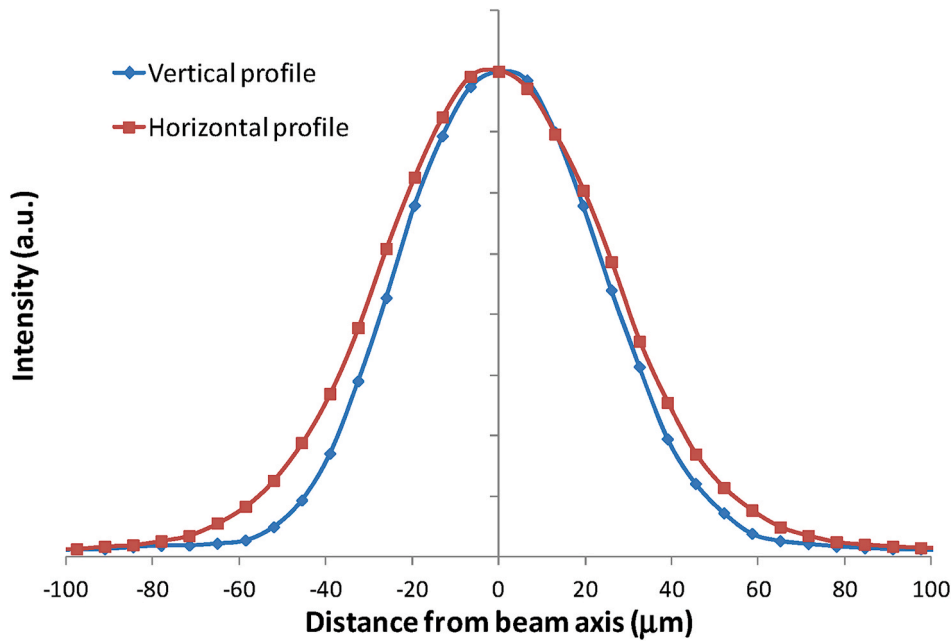

Fig. 4. Intensity profile of the laser beam in the focal plane. Beam diameters (FWHM) 62 μm (horizontal), 54 μm (vertical).

of incident energy are shown in Fig. 5.

The incident energy was corrected for the value of the Fresnel reflection at the sample interface.

At each energy level, the transmission $T(z)$ (Z-scan curve) is fitted with the expected transmission function, to calculate an amplitude coefficient A, proportional to the pulse energy, to the n_2 coefficient and to the sample length L, i.e.

$$T(z) = 1 + A \times F(z/z_r) \tag{1}$$

Where

$$A(E) = K \times E \times L \times n_2 \tag{2}$$

z_r is a characteristic diffraction distance. The function $F(z/z_r)$

depends only on the beam structure [20] whereas the coefficient K depends on the pulse time profile and on the beam cross section at focus. The derivation of Eqns (1) and (2) is exposed in Appendix 1, along with the numerical approximations used for the data analysis.

The value of $A(E)$ for different values of incident energy E is fitted for the sample and the standard with the linear relationship

$$A(E) = c \times E \tag{3}$$

This is exemplified in the Fig. 6 below.

Finally, the n_2 of the sample is calculated from the ratio of the slopes for the sample and the standard, with the equation:

$$n_{2Sample} = \frac{c_{Sample}}{c_{Standard}} \frac{L_{Standard}}{L_{Sample}} n_{2Standard} \tag{4}$$
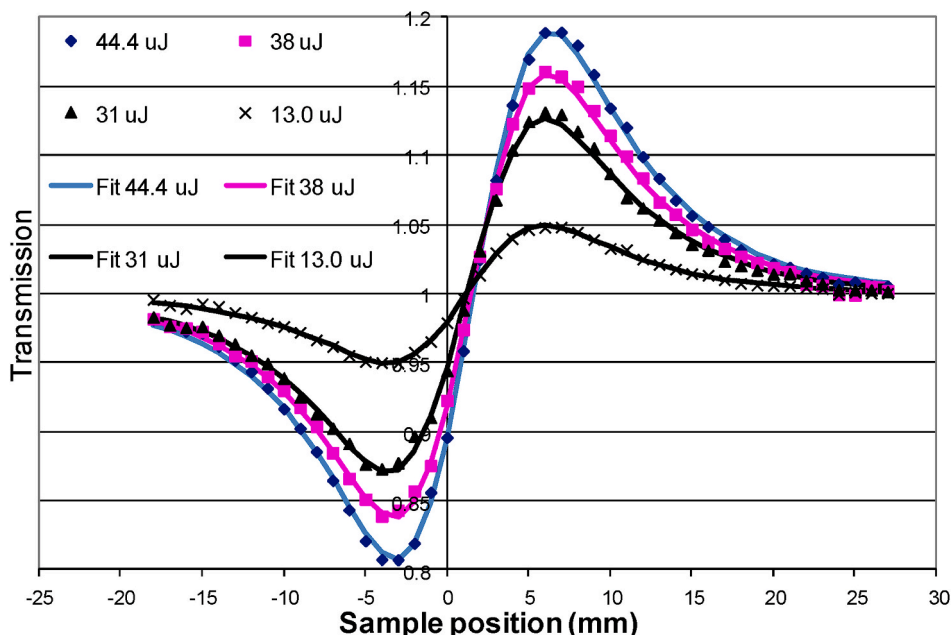
Fig. 5. Z-scan traces obtained from one of the Yb:YAG ceramic samples at different levels of incident energy. The origin of the horizontal axis corresponds to about the position of the focus of the beam. The vertical axis is the transmission through the pinhole placed on the beam axis. The linear transmission value (i.e. very far from focus) is normalized to 1 for all the energy levels.
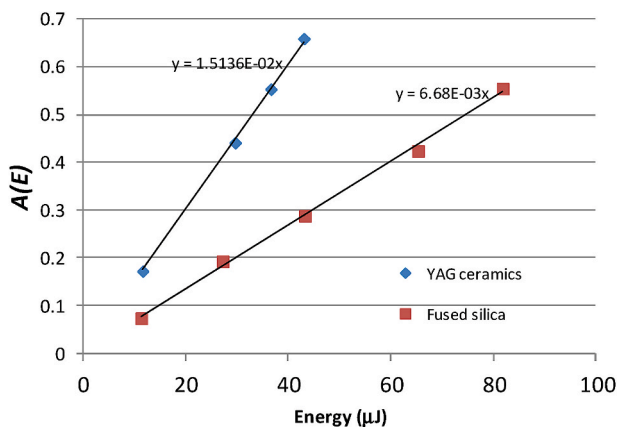

Fig. 6. Value of the proportionality coefficient A(E) for different values of incident energy for one of the YAG samples and for the fused silica reference.

3.2. Time-resolved digital-holographic (TRDH) microscopy technique

The sketch of TRDH experimental setup is shown in Fig. 7. The Yb:KGW based laser source is used as a pump which generates femtosecond light pulses centered around 1030 nm wavelength. The light is split into two paths by using a polarizing beam splitter. One path is then directed into a non-collinear optical parametric amplifier (NOPA) and is used as a probe. Here, light is split again and white light supercontinuum together with the 3rd harmonic (343 nm) are generated. The third harmonic is then used within β-barium borate (BBO) crystal to amplify the fraction of the supercontinuum spectrum. The amplified probe (centered around 525 nm) is then compressed down to ~30 fs FWHM duration by using fused silica prisms. Pulse durations of pump and probe pulses were characterized by using a second-harmonic scanning autocorrelator. The half-wave plate is then used to set the polarization to vertical with respect to the surface of the optical table. It is further directed towards a mechanical delay line and Mach–Zehnder interferometer, where is used for holographic-microscopic probing of a light-induced transparent object. To compensate for the group delay dispersion between interferometer branches due to the glass of microscope objective the similar amount of glass was inserted into the reference branch. It was then fine-tuned with a pair of fused quartz prisms. To extend spatial-temporal overlapping of short probing pulses (both object and reference) a diffraction grating was also used within the reference branch. The grating produces a tilt of wavefront extending the area of high interference contrast on CCD1. To obtain high enough spatial resolution of the light-induced object a $0.4 \times NA$ and $20 \times$ microscope objective was used inside the interferometer. An active area of CCD2 camera served as a reference plane. The second path of laser light is used as a pump in the n_2 evaluation experiments. It is directed towards the sample through multiple steering mirrors to match the long optical path that the probe pulse passes inside the NOPA. The pump energy is adjusted with half waveplates and polarizing beam splitter and directed into the entrance surface of a sample by using a 15 cm focal length lens. The beam was focused behind the entrance surface, namely 370 μm for Nd:CaF$_2$ and 540 μm for Yb:YAG. Both the pumping and the probing pulses were overlapped inside the transparent sample perpendicularly to each other. The propagating object is parallel to the surface of the optical table. During the experiments, an interferometric response of a transparent light-induced phase-contrast object is registered in the form of a numerical hologram on CCD1. After the numerical reconstruction of the digital hologram, the complex amplitude field of view corresponding to an area of 200×200 μm^2 is obtained. The excitation was observed in multiple temporal steps of 50 fs from the moment the light enters the field of view up to 1 ps probe delay. The experiments for the two materials were done on two separate occasions. The characteristic parameters of the two experiments summarized in Table 1.

The diameter of pumping pulses was characterized by using imaging objective and CCD camera.

As mentioned before the response of the material was recorded via a digital-holographic approach. The probing pulse passes the object and collects pump intensity-dependent change in the refractive index and thus a delay of the wavefront. This effect is known as cross-phase modulation. A distorted interference pattern is registered out of focus on the CCD1 camera and is later used to reconstruct the amplitude and phase of the probe field numerically [26]. The algorithm is based on
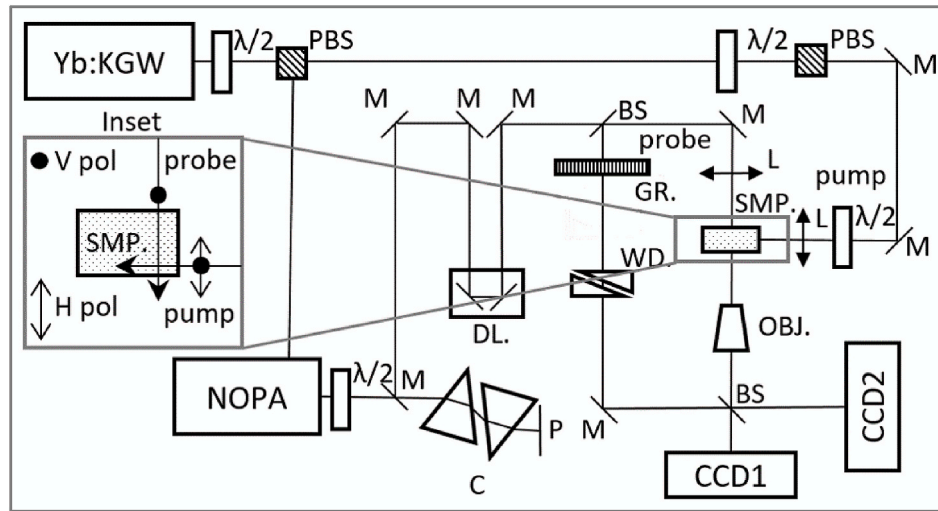
Fig. 7. TRDH experimental setup. PBS - polarizing beam splitter, M − mirrors, BS - neutral beam splitters, P - periscope, C - prism compressor, GR - diffraction grating, WD - glass wedges, OBJ – microscope objective, SMP - sapphire sample, Tl - telescope, DL – delay line, CDD1 - holography registration, CDD2 - object view.

Table 1
The characteristic parameters of pump and probe in two separate experiments.

Pump	Nd:CaF$_2$	YAG
Wavelength (nm)	1030	1030
Duration, FWHM (fs)	390	420
Focal spot diameter (µm), 1/e^2	59	51
Probe		
Wavelength (nm)	525	525
Duration (fs)	33	33

light diffraction and implemented via fast Fourier transformation. During the experiment time-dependent nonlinear response of the samples to light polarized vertically (V) and horizontally (H) were measured.

To evaluate the nonlinear refractive index, a numerical model of propagation is employed and directly compared to the experimental data. The evaluation is done by using split-step method. The nonlinear Schrödinger equation (5) is used to model pump propagation, while (6) was used for probe pulse propagation through the excited medium. The calculations were done assuming both pulses initially could be defined as 3-dimensional Gaussian functions in spatial coordinates and represented on a 3-dimensional numerical grid.

$$\frac{\partial E_1}{\partial z} = \frac{i}{2k_1}\left(\frac{\partial^2 E_1}{\partial x^2} + \frac{\partial^2 E_1}{\partial y^2}\right) + iC_1|E_1|^2 E_1 - \frac{1}{u_{01}}\frac{\partial E_1}{\partial t} \tag{5}$$

$$\frac{\partial E_2}{\partial z} = \frac{i}{2k_2}\left(\frac{\partial^2 E_2}{\partial x^2} + \frac{\partial^2 E_2}{\partial y^2}\right) + iC_2|E_1|^2 E_2 - \frac{1}{u_{02}}\frac{\partial E_2}{\partial t} + \frac{g_{02}}{2}\frac{\partial^2 E_2}{\partial t^2} \tag{6}$$

$$C_1 = ck_1\varepsilon_0 n_2/2 \tag{7}$$

$$C_2 = ck_2\varepsilon_0 n_2 \tag{8}$$

Here $E_{1,2}$ is a complex amplitude of the electric field, x, y, z, t space, and time coordinates, i imaginary unit, C nonlinear focusing coefficient, I intensity, u_0 group velocity, g_0 group velocity dispersion coefficient, c speed of light in vacuum, k wave number in medium, ε_0 vacuum permittivity, n_2 - nonlinear refractive index. The 1 and 2 denote parameters of pump or probe, respectively. The self-focusing parameter C_1 and cross-phase modulation coefficient C_2 differ by a multiplier of 2 for V–V polarization as in equation (8) and 2/3 for H–V polarized pump-probe (not shown), due to cross-phase modulation dependence on polarization in isotropic media assuming anisotropy is small.

In the case of pump-pulse, group velocity dispersion and cross-phase modulation are negligible since the spectrum of the pump pulse is

narrow and probe pulse intensity is low. Therefore, they are not included in the calculations. In the case of probe-pulse, the self-induced modulation can also be neglected due to low intensity. However, as it is relatively short, the duration of the pulse is affected by group velocity dispersion. Here, cross-phase modulation is of high importance, since the pump-pulse produces high intensities and the experimentally registered signal is essential. To avoid more complexity nonlinear absorption was also not included since the experiment conditions are chosen so that the intensity of the pump pulse is below the threshold of free-electron generation in the area of interest. The calculations for pump and probe can be done separately while tracking the relative positions of both and accounting for cross-phase modulation where they overlap. A resulting phase shift due to cross-phase modulation is evaluated, by calculating the average phase shift of different probe time slices, where the probe intensity at the center exceeds $1/e^2$ of peak intensity. The results of both experiments corresponding to numerical simulations are given in Fig. 8. Similar experiments were performed on fused silica samples, where n_2 of 2.68×10^{-20} m^2/W was obtained and could be used as a reference.

3.3. Degenerate Four wave mixing (DFWM) technique

The Degenerate Four Wave Mixing (DFWM) scheme is based on the measurement of the amplitude of the diffracted light from a two beam intersection in the sample, this measurement being next compared with those obtained on a standard sample with a well-known non-linearity n_2. The scheme is shown in Fig. 9. There are a couple of possibilities for a four-wave mixing arrangement. Here a simple two incident wave approach, also known as self-diffraction geometry is used, which is typically also applied for third order FROG (Frequency Resolved Optical Gating) pulse characterization measurements [31]. The application of ultrashort broad bandwidth pulses and relatively thin samples do not require exact phase matching conditions as could be achieved with the so called folded boxcars geometry or the phase conjugation geometry.

The delay of the two pulses against each other that is formed by mirrors M2 and M3 can be used for temporal resolution as well as for background suppression. The latter is made possible since only the temporally and spatially overlapping pulses generate the signal. As the de-facto standard fused silica is used, this material being one of the most investigated and additionally available with high purity. The effect of this self-diffraction comes from a grating that is produced by the two beams that interfere inside the sample. The spatial intensity variation produces a phase grating through the third order nonlinear refractive
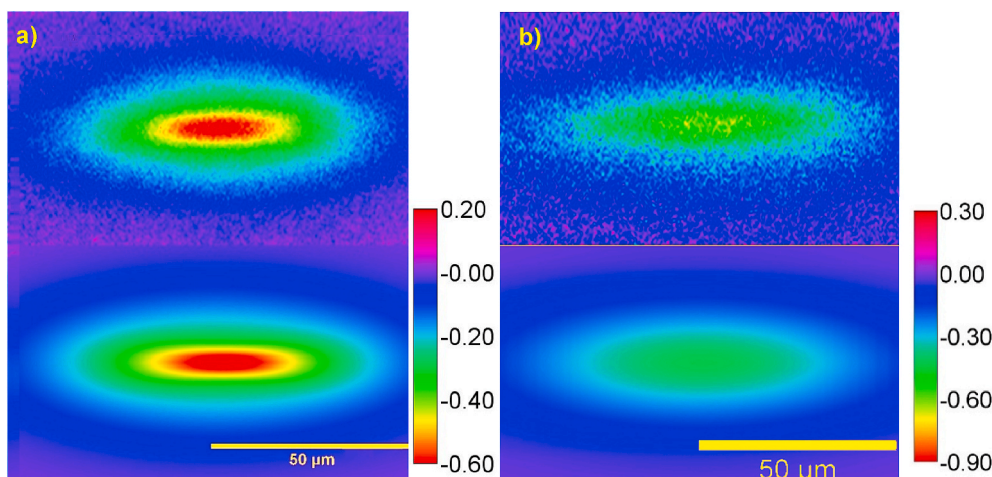
Fig. 8. Experiment vs. model fora) Yb/YAG sample at 4.2 μJ and 500 μm resulting n2 $= 6.02 \times 10^{-20}$ m^2/W; b) Nd:CaF$_2$ sample at 14 μJ 370 μm resulting $n_2 = 3.8 \times 10^{-20}$ m^2/W.
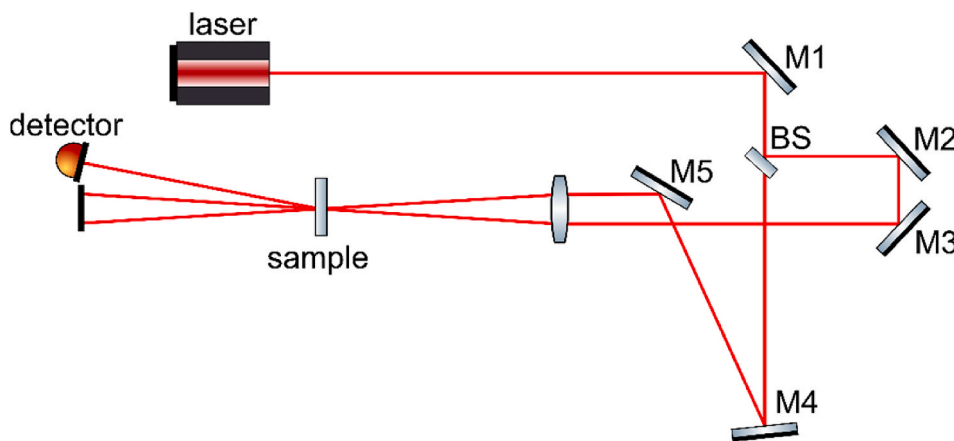

Fig. 9. Degenerate four wave mixing scheme in self-diffraction geometry for the determination of the third order nonlinear coefficients. BS is a beam splitter, M1-5 are turning mirrors, where the mirrors M3 and M2 are placed on a linear stage for delaying one pulse against the other.

index.

Since in the small amplitude case, where the variation of the incident beams through the nonlinear effect is neglected, the diffraction efficiency is proportional to the grating amplitude, the amount of diffracted light is linearly linked to the materials n_2. Moreover the sample thickness L gives origin to a quadratic dependence on L^2.

To prove the validity of the dependencies, measurements at a wavelength of 1030 nm with a pulse width of 150 fs were conducted for a couple of different sample thicknesses made of fused silica. The result is depicted in Fig. 10 as uncorrected measurement points (in blue). It appears that the deduced nonlinear coefficient reduces with longer sample lengths. This is related to two effects: i) The beam overlap can only be guaranteed for a certain travelling range and ii) The phase mismatch will come into play after a certain distance in the sample.

Both of these effects depend also on the linear refractive index of the sample, since refraction occurs at the sample front surface which changes the angle between the beams and additionally, the changed wavelength will have an impact on the phase matching condition. If samples are not antireflective-coated, Fresnel-reflection must also be taken into account if different samples should be compared. All these effects are considered and therefore included in the measurement procedure. The effect is shown in Fig. 10, where corrected measurement points (red) are compared to the uncorrected ones (blue).

Finally, Fig. 11 reports measurements of different materials, namely Nd:Lu:CaF$_2$, Yb:YAG-ceramics together with the reference fused silica,
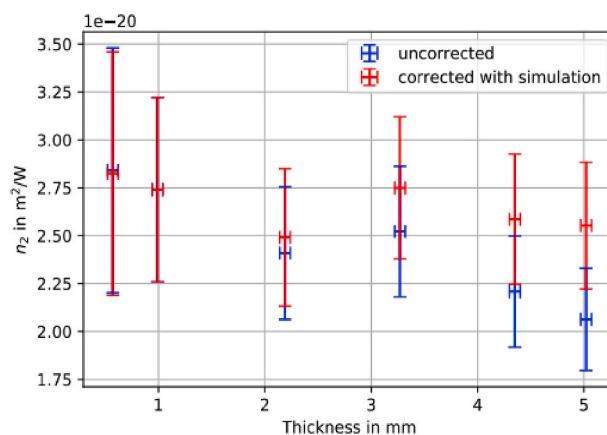

Fig. 10. Measurement of the n$_2$ of fused silica using different sample thicknesses. The blue curve shows uncorrected values and the red ones are the corrected values according to the phase matching and beam overlapping. (For interpretation of the references to colour in this figure legend, the reader is referred to the Web version of this article.)
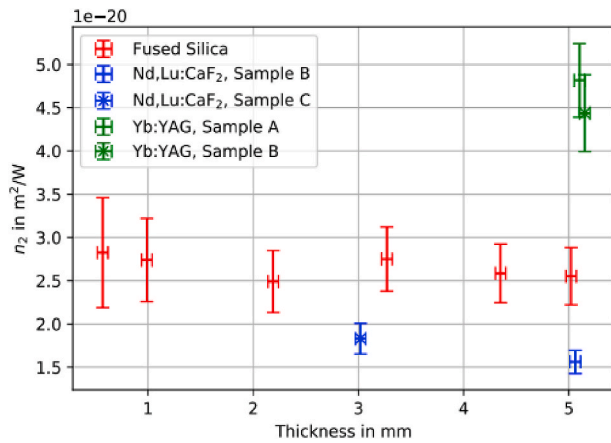
Fig. 11. DFWM measurements on Yb:YAG ceramics and Nd:Lu:CaF₂compared with the reference measurement on fused silica for different sample thicknesses.

for different thicknesses. After correction from the effects above one can see that there is no thickness dependence within the error-bars left. The results are reported in next section in comparison with the results from other techniques.

4. Results and discussion

Experimental errors have been estimated and they are in the range 6–13% for all techniques and samples.

The estimations of n_2 values for the different samples obtained from the different techniques are reported in the Table 2, synthesized in Table 3 and then discussed in the following sub-sections.

4.1. Reference

The set-ups presented in previous section were first calibrated in comparison with well-known material, *e.g.* fused silica. As for the value of the nonlinear refractive index n_2 of fused silica, an extensive review of the reported values in literature was carried out. Then the average value of the literature data (weighted with the reported measurement uncertainties) was calculated. The error was calculated as the weighted average of the literature errors. This is summarized in the Table 4.

The most recent reference on this subject is probably the Milam's paper [37], were an accurate analysis of a broad data set from previous literature data was carried out (including references in Table 4). In this

Table 2

Non-linear refractive index values determined at 1 μm and 800 nm for Nd:CaF₂ crystals and Yb/YAG ceramics from different techniques. (*Absolute measurements. n_2 of 2.68×10^{-20} m²/W was also measured for fused silica).

	Technique	Nd:CaF₂ (10^{-20} m²/W)	Yb:YAG (10^{-20} m²/W)
A1.	Z-scan (@ 1064 nm) Sample A	1.95	7.4
A2.	Z-scan (@ 1064 nm) Sample B	2.10	7.4
B1.	Z-scan (@ 800 nm) Sample A	2.2	8.6
B2.	Z-scan (@ 800 nm) Sample B	2.5	7.4
C1.	DFWM (@ 1030 nm) Sample A		4.82
C2.	DFWM (@ 1030 nm) Sample B	1.56	4.44
C3.	DFWM (@ 1030 nm) Sample C	1.83	
C4.	DFWM (@ 800 nm) Sample C	2.27	
D.	TRDH* (@ 1030 nm) Sample B	3.8	6.02

Table 3

Mean value, standard deviation and relative deviation of non-linear refractive index values determined at 1 μm and 800 nm for Nd:CaF₂ crystals and Yb/YAG ceramics.

	Mean value (10^{-20} m²/W)	Standard deviation (10^{-20} m²/W)	Relative deviation
Nd:CaF₂ at 1 μm	2.25	0.89	0.40
Nd:CaF₂ at 800 nm	2.32	0.16	0.07
Yb:YAG at 1 μm	6.02	1.39	0.23
Yb:YAG at 800 nm	8.00	0.85	0.11

Table 4

Review of the literature values of n_2 for fused silica at 1064 nm, and calculation of their weighted variance.

Source	Value of n_2 (x10^{-20} m²/W)	Reported error (x10^{-20} m²/W)
[32]	2.46	0.37
[33]	2.14	0.43
[34]	2.73	0.27
[35]	3.93	1.97
[36]	2.14	0.43
[37]	**2.74**	**0.17**

latter, the n_2 value of fused silica is provided at 1053 nm and is (2.74 ± 0.17)x10^{-20} m²/W. We then chose this value as reference at 1064 nm and at 1030 nm considering that the dispersion is negligible for such a small wavelength variation.

At 800 nm, a linear interpolation between the values of the Milam's paper, i.e. 2.74 at 1053 nm and 3.0 at 527 nm gives 2.87×10^{-20} m²/W at 800 nm, i.e. a difference of 5% with the value at 1053 nm.

4.2. Repeatability

A perturbation theory analysis, known as PERT [38] and proposed for the dispersion of the nonlinear refractive index showed first that discrepancies are mainly due to sample to sample dispersion. The dispersion was also assessed in our approach, first considering the repeatability issue. The definition of the repeatability considers here the application of the same procedure on the same set-up but on different samples.

To this purpose, two different Nd:CaF₂ crystals and also two Yb:YAG ceramics were measured. From z-scan techniques, the repeatability shows discrepancies up to 7% (comparison of results A1 and A2 in Tables 2) and 15% (comparison of results B1 and B2 in Table 2) from measurements obtained at 1030 nm and 800 nm, respectively. The repeatability is estimated at also 15% from DFWM technique (comparison of results C2 and C3 in Table 2). Therefore, considering that error bars are about 10%, it seems that sample to sample dispersion moderately contributes to measurement repeatability.

4.3. Reproducibility

From results reported in Table 2, specifically comparing A1/A2 and B1/B2, the reproducibility can also be assessed. The definition of the reproducibility considers here the application of the same procedure on different set-ups. It is first considered that non-linear index at 1030 and 800 nm should be very close. As mentioned in paragraph 4.1 differences, lower than 5% are estimated. To emphasize this point, we can also refer to Fig. 7 of [23]. In our work, reproducibilities about 15% and 8% were obtained for Nd:CaF₂ crystals and Yb:YAG ceramics, respectively.

4.4. Synthesis

The average values, the dispersion of the data from the different techniques and configurations are displayed in the Table 3. First the mean values and standard deviations at 1 μm are $(2.25\pm0.89)\times10^{-20}$ m^2/W and $(6.02\pm1.39)\times10^{-20}$ m^2/W for Nd:CaF$_2$ crystals and Yb:YAG ceramics, respectively, and $(2.32\pm0.16)\times10^{-20}$ m^2/W and $(8.00\pm 0.85)\times10^{-20}$ m^2/W at 800 nm. Relative deviations are in the range [7–40%]. They are much larger than error bars estimated for each procedure (lower than 13%). These values are as dispersed as those generally observed in the literature.

4.5. Comparison with literature

The values measured here are compared with those already reported in literature.

For CaF$_2$ crystals measured at 1064 nm, Milam [34] reported value of 1.90×10^{-20} m^2/W for pure CaF$_2$ crystal. This value is lower about 17% than the one reported in this work but we notice also that the literature value is relative to undoped CaF$_2$. Therefore the difference could be attributed to the Nd doping or to the Lu co-doping. Nonetheless we note that this difference is very close to the reproducibility obtained in this work (15%) and also in the range of the relative deviations [7–40%] which means that it is not possible to really conclude.

For Yb:YAG ceramics at 1064 nm, Smith [35] and Adair [32] reported values of 8.15×10^{-20} m^2/W and 6.23×10^{-20} m^2/W respectively. We note that these measurements were obtained on crystals.

5. Conclusions

In order to characterize precisely new laser materials in terms of nonlinear index of refraction, four different set-ups have been developed together with three different procedures, namely Z-scan, DFWM and TRDH were applied at different wavelengths. This approach allowed the comparison of experimental n_2 estimation and at the end reducing the intervals of confidence on data. The n_2 values for Neodymium-doped CaF$_2$ crystals and for Yb:YAG ceramics were defined more precisely, and measured respectively at 1 μm: $(2.25\pm0.89)\times10^{-20}$ m^2/W and $(6.02\pm1.39)\times10^{-20}$ m^2/W, and at 800 nm: $(2.32\pm0.16)\times10^{-20}$ m^2/W and $(8.00\pm0.85)\times10^{-20}$ m^2/W. This comparison of experimental results (kind of round-robin) using different facilities is original and without precedent, and it will increase the accuracy of n_2 values determination.

CRediT authorship contribution statement

Laurent Lamaignère: Conceptualization, Methodology, Writing - original draft. **Guido Toci:** Data curation, Writing - original draft. **Barbara Patrizi:** Data curation. **Matteo Vannini:** Data curation. **Angela Pirri:** Data curation. **Samuele Fanetti:** Data curation. **Roberto Bini:** Data curation. **Gabriel Mennerat:** Data curation, Writing - original draft. **Andrius Melninkaitis:** Data curation, Writing - original draft. **Luise Lukas:** Data curation. **Joachim Hein:** Data curation, Writing - original draft.

Declaration of competing interest

The authors declare that they have no known competing financial interests or personal relationships that could have appeared to influence the work reported in this paper.

Acknowledgements

Appendix. 1– Derivation of the transmission *T(z)* in the thin sample limit, for a trimmed Airy beam

A1.1 – Derivation of T(z)

The theory of the z-scan measurements with circularly symmetric beams (of which the trimmed Airy beam is a special case) has been described in details in [20]. We recall here the main elements, used to derive Eqns (1)–(3), along with the results of some specific numerical approximations used for computational and fitting purposes.

In a z-scan experiment a collimated laser beam at wavelength λ is focused on the sample with a lens with focal length *f*. In the Fresnel condition, the beam amplitude distribution near the focal plane of the lens can be calculated with a Fourier transform (which in the case of cylindrical coordinates becomes a Hankel transform) with the expression

$$\mathscr{E}(r,z) = \frac{1}{\lambda f}\int_0^{r_a}\mathscr{E}_{lens}^0 g(r_{lens})J_0\left(\frac{2\pi\, r\, r_{lens}}{\lambda f}\right)exp\left[\frac{-i\pi z}{\lambda}\left(\frac{r_{lens}}{f}\right)^2\right]2\pi\, r_{lens}\, dr_{lens} \tag{A1}$$

where r_{lens} is the radial coordinate from the beam axis on the lens plane, $\mathscr{E}_{lens}^0$ is the peak electric field, and $g(r_{lens})$ is the electric field amplitude distribution in the lens plane corresponding to the Airy function (normalized to 1 at the peak), z is the coordinate along the lens axis (z = 0 corresponding to the focal plane), J_0 is the zero-order Bessel function, *r* is the radial distance from the lens (and beam) axis, r_a is the radius of the first zero of the Airy intensity distribution.

It is convenient to introduce the parameters $z_r = (\lambda f^2)/(\pi r_a^2)$ (a diffraction distance analogous to the Rayleigh range for a Gaussian beam), $w = (\lambda f)/(\pi r_a)$ (related to the spot radius in the beam waist) and the change of variable $\rho = r_{lens}/r_a$ so that Eq. (A1) takes the form

$$\mathscr{E}(r,z) = \frac{2r_a E_{lens}^0}{w}\int_0^1 g(\rho r_a)J_0\left(\frac{2 r\rho}{w}\right)exp\left[\frac{-iz}{z_r}\rho^2\right]\rho d\rho = \mathscr{E}_0[f_r(r,z) + if_i(r,z)] \tag{A2}$$

where $\mathscr{E}_0$ is the peak amplitude of the electric field in the focal plane (i.e. at *r = 0, z = 0)* , f_r and f_i as the real and imaginary parts of the electric field distribution, normalized so that $f_r(0,0) = 1$ and $f_i(0,0) = 0$.

We introduce the nonlinear phase shift on the focal plane and on the beam axis as $\Delta\Phi = kn_2I_0L$ and $\Delta\Psi = (\beta/2)I_0L$, where I_0 is the intensity on the

beam axis in the focal plane, k is the wavenumber, n_2 is the Kerr coefficient, β is the two photon absorption coefficient and L is the sample length. Linear absorption has been considered negligible. The electric field distribution at the output of a thin sample can be written as

$$\mathscr{E}_{out}(r,z) = \mathscr{E}_0[(f_r - f_r I\Delta\Psi - f_i I\Delta\Phi) + i(f_i - f_i I\Delta\Psi + f_r I\Delta\Phi)] \tag{A3}$$

Where $I = f_r^2 + f_i^2$.

The electric field amplitude distribution in the far field (i.e. at a long distance d from the focal plane) can be calculated as the two-dimensional Fourier transform of the electric field distribution at the sample output. On the beam axis, this simply reduces to the surface integral of $\mathscr{E}_{out}$, i.e.

$$\mathscr{E}(r=0, \; z=d \gg z_r) = \frac{1}{\lambda d}\int \mathscr{E}_{out}\, ds \tag{A4}$$

The transmission of a small aperture on the far field and on the beam axis is simply proportional to the ratio between the square modulus of the electric field (Eq. (A4)), which can be calculated using Eqn. (A2) and (A3). Keeping only the first order terms in $\Delta\Phi$ and $\Delta\Psi$, noting that when the electric field profile on the lens has an expansion of only even powers of r_{lens} it is $\int f_i ds = 0$ and $\int f_r ds$ is a constant [20], we obtain for the normalized transmission of the on-axis aperture the expression

$$T(z) = 1 - \frac{2\int f_i I ds}{\int f_r ds}\Delta\Phi \; - \frac{2\int f_r I ds}{\int f_r ds}\Delta\Psi = 1 + F(z/z_r)\Delta\Phi \; + G(z/z_r)\Delta\Psi \tag{A5}$$

The function $F(z/z_r)$ is the one appearing in Eq. (1). The calculation of the functions $F(z/z_r)$ and $G(z/z_r)$ in Eq. (A5) can be carried out numerically following the steps outlined above.

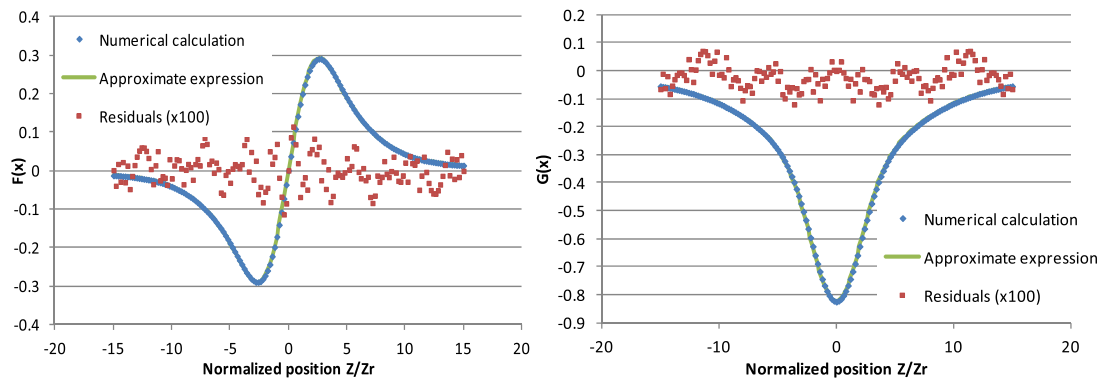### A1.2 – Numerical approximations

As the evaluation of $F(z/z_r)$ and $G(z/z_r)$ is computationally expensive and difficult to implement in a numerical fitting routine, we have devised numerical expressions that closely approximate these two functions over a broad range of values of z/z_r , and are more convenient for computational purposes.

The two functions F and G can be approximated as a ratio of polynomials, in the form

$$\tilde{F}(x) = sign(x)\left[\sum_{i=1}^{4} a_i|x|^i \; / \; \sum_{i=0}^{5} b_i|x|^i\right] \tag{A6}$$

$$\tilde{G}(x) = \left[\sum_{i=0}^{4} c_i|x|^i \; / \; \sum_{i=0}^{5} d_i|x|^i\right] \tag{A7}$$

The results of these approximations are shown in Fig. A1. It can be seen that the deviation of the numerical approximations is less than 0.3% for F and less than 0.13% for G, so the inaccuracy that is introduced by the use of these expression is negligible with respect to the other sources of experimental error.

Fig. A1. Comparison between the numerical evaluations for the functions F and G (Eq. (A5)) and the approximated forms $\tilde{F}$ and $\tilde{G}$. The residuals are the differences between the results of the two methods of evaluation, magnified by 100.

The coefficients for the calculations of the expressions (A6) and (A7) are reported in the table below.

Table A1
Coefficients for the evaluation of the expressions (A6) and (A7), in the range $-15 < x < 15$

i	A	b	c	d
0	-	1	-0.82500119	1
1	0.193097320	-0.074489830	0.22073425	-0.26178596
2	-0.033450640	-0.001907530	-0.02978765	0.09664783
3	0.001955207	0.022524377	0.000691125	-0.01033912
4	-0.000033880	-0.003128500	-0.00003662	0.000655813
5	-	0.000134898	-	0.000065886

A1.3 – Expressions for time integrated T(z)

Finally, we note that in an experiment carried out with short laser pulses (in the tens of ps range or shorter) what is actually measured are the incident pulse energy E and the energy transmitted through the pinhole, rather than the instantaneous power or intensity. It is then useful to consider how the time averaged (energy) transmission is related to the instantaneous transmission described by Eq. (A5).

We then introduce a pulse temporal profile function $p(t)$ so that the beam intensity in the focus and the beam intensity on the pinhole aperture evolve in time respectively as $I_0(t) = I_0 p(t)$, $I_{Ph}(t) = I_{Ph0} p(t)$, (with I_0, I_{Ph0} the peak values for these quantities, $p(t)$ is dimensionless). The energy transmission through the pinhole, normalized to the value measured when the sample is very far from the focus (i.e. when the nonlinear effect is negligible) at a given sample position is then:

$$T(z) = \frac{I_{Ph0}\left[\int_{pulse}p(t)dt + (F(z/z_r)kn_2L + G(z/z_r)(\beta/2)L)I_0\int_{pulse}p(t)^2dt\right]}{\left[I_{Ph0}\int_{pulse}p(t)dt\right]} \tag{A8}$$

Considering that I_0 is proportional to the incident pulse energy E through

$$I_0 = E \, / \left[S\int_{pulse}p(t)dt\right] \tag{A9}$$

where S is the effective beam area in the focal plane, the equation (A8) can be written as

$$T(z) = 1 + F\left(\frac{z}{z_r}\right)\left\{k\frac{\int_{pulse}p(t)^2dt}{S\left(\left[\int_{pulse}p(t)dt\right]\right)^2}\right\}ELn_2 + G\left(\frac{z}{z_r}\right)EL\left(\frac{\beta}{2}\right)\left\{\frac{\int_{pulse}p(t)^2dt}{S\left(\left[\int_{pulse}p(t)dt\right]\right)^2}\right\} \tag{A10}$$

It can be seen that Eq. (A10) corresponds to Eqns (1) and (2) with

$$A(E) = \left\{k\frac{\int_{pulse}p(t)^2dt}{S\left(\left[\int_{pulse}p(t)dt\right]\right)^2}\right\}ELn_2 = KELn_2 \tag{A11}$$

where the coefficient K depends on the pulse temporal profile and beam cross section in the focal plane.

References

[1] S.P.D. Mangles, C.D. Murphy, Z. Najmudin, A.G.R. Thomas, J.L. Collier, A. E. Dangor, E.J. Divall, P.S. Foster, J.G. Gallacher, C.J. Hooker, D.A. Jaroszynski, A. J. Langley, W.B. Mori, P.A. Norreys, F.S. Tsung, R. Viskup, B.R. Walton, K. Krushelnick, Monoenergetic beams of relativistic electrons from intense laser-plasma interactions, Nature 431 (7008) (2004) 535–538.
[2] H. Schwoerer, S. Pfotenhauer, O. Jäckel, K.U. Amthor, B. Liesfeld, W. Ziegler, R. Sauerbrey, K.W.D. Ledingham, T. Esirkepov, Laser-plasma acceleration of quasi-monoenergetic protons from microstructured targets, Nature 439 (7075) (2006) 445–448.
[3] S. Kneip, S.R. Nagel, C. Bellei, N. Bourgeois, A.E. Dangor, A. Gopal, R. Heathcote, S. P.D. Mangles, J.R. Marquès, A. Maksimchuk, P.M. Nilson, K.T. Phuoc, S. Reed, M. Tzoufras, F.S. Tsung, L. Willingale, W.B. Mori, A. Rousse, K. Krushelnick, Z. Najmudin, Observation of synchrotron radiation from electrons accelerated in a petawatt-laser-generated plasma cavity, Phys. Rev. Lett. **100** (10) (2008), 105006.
[4] G. Toci, Z. Mazzotta, L. Labate, F. Mathieu, M. Vannini, B. Patrizi, L.A. Gizzi, Conceptual design of a laser driver for a plasma accelerator user facility, Instruments 3 (2019) 40.
[5] M.K. Weikum, T. Akhter, D. Alesini, A.S. Alexandrova, M.P. Anania, N.E. Andreev, I.A. Andriyash, A. Aschikhin, R.W. Assmann, T. Audet, et al., Status of the Horizon 2020 EuPRAXIA conceptual design study, J. Phys. Conf. Ser. 1350 (2019), 12059.
[6] M. Dunne, A high-power laser fusion facility for Europe, Nat. Phys. 2 (1) (2006) 2–5.
[7] G. Miller, E. Moses, C. Wuest, The national ignition facility, Opt. Eng. 43 (12) (2004) 2841–2853.
[8] P.D. Mason, M. Fitton, A. Lintern, S. Banerjee, K. Ertel, T. Davenne, J. Hill, S. P. Blake, P.J. Phillips, T.J. Butcher, J.M. Smith, M. De Vido, R.J.S. Greenhalgh, C. Hernandez-Gomez, J.L. Collier, Scalable design for a high energy cryogenic gas cooled diode pumped laser amplifier, Appl. Optic. 54 (13) (2015) 4227–4238.
[9] S. Banerjee, K. Ertel, P.D. Mason, P.J. Phillips, M. De Vido, J.M. Smith, T. J. Butcher, C. Hernandez-Gomez, R.J.S. Greenhalgh, J.L. Collier, DiPOLE: a 10 J, 10 Hz cryogenic gas cooled multi-slab nanosecond Yb:YAG laser, Optic Express 23 (15) (2015) 19542–19551.
[10] Y. Senatsky, A. Shirakawa, Y. Sato, J. Hagiwara, J. Lu, K. Ueda, T. Yanagitani, Nonlinear refractive index of ceramic laser media and perspectives of their usage in a high-power laser-driver, Laser Phys. Lett. 1 (10) (2004) 500.
[11] J.L. Doualan, L.B. Su, G. Brasse, A. Benayad, V. Ménard, Y.Y. Zhan, A. Braud, P. Camy, J. Xu, R. Moncorgé, Improvement of infrared laser properties of Nd:CaF$_2$ crystals via codoping with Y^{3+} and Lu^{3+} buffer ions, JOSA B 30 (2013) 3018.

[12] S. Normani, A. Braud, R. Soulard, J.L. Doualan, A. Benayad, V. Menard, G. Brasse, R. Moncorgé, J.P. Goossens, P. Camy, Site selective analysis of Nd^{3+}- Lu^{3+} codoped CaF$_2$ laser crystals, Crystal Engineering Communications 18 (2016) 9016.
[13] A. Lucca, M. Jacquemet, F. Druon, F. Balembois, P. Georges, P. Camy, J.L. Doualan, R. Moncorgé, High-power tunable diode-pumped Yb3+:CaF2 laser, Opt. Lett. 29 (2004) 1879–1881.
[14] M. Siebold, M. Hornung, R. Boedefeld, S. Podleska, S. Klingebiel, C. Wandt, F. Krausz, S. Karsch, R. Uecker, A. Jochmann, J. Hein, M.C. Kaluza, Terawatt diode-pumped Yb:CaF$_2$ laser, Opt. Lett. 33 (2008) 2770–2772.
[15] J. Körner, V. Jambunathan, J. Hein, R. Seifert, M. Loeser, M. Siebold, U. Schramm, P. Sikocinski, A. Lucianetti, T. Mocek, M.C. Kaluza, Spectroscopic characterization of Yb3+-doped laser materials at cryogenic temperatures, Appl. Phys. B 116 (2014) 75.
[16] M. Hornung, H. Liebetrau, S. Keppler, A. Kessler, M. Hellwing, F. Schorcht, G. A. Becker, M. Reuter, J. Polz, J. Körner, J. Hein, M.C. Kaluza, 54 J pulses with 18 nm bandwidth from a diode-pumped chirped-pulse amplification laser system, Optic Lett. 41 (2016) 5413.
[17] M.D. Perry, T. Ditmire, B.C. Stuart, Self-phase modulation in chirped-pulse amplification, Opt. Lett. 19 (1994) 2149–2151.
[18] H. Liebetrau, M. Hornung, A. Siedel, M. Hellwing, A. Kessler, S. Keppler, F. Schorcht, J. Hein, M.C. Kaluza, Ultra-high contrast frontend for high peak power fs-lasers at 1030 nm, Optic Express 22 (2014), 24776.
[19] M. Sheik-Bahae, A.A. Said, T.H. Wei, D.J. Hagan, E.W. Van Stryland, Sensitive measurement of optical nonlinearities using a single beam, IEEE J. Quant. Electron. 26 (4) (1990) 760–769.
[20] B.K. Rhee, J.S. Byun, E.W. Van Stryland, Z scan using circularly symmetric beams, JOSA B 13 (12) (1996) 2720–2723.
[21] G. Toci, M. Vannini, R. Salimbeni, M.A. Dubinskii, E. Giorgetti, First Z-scan n2 measurements on crystal hosts for ultraviolet laser systems, Appl. Phys. B 71 (2000) 907.
[22] E. Giorgetti, G. Toci, M. Vannini, Nonlinear characterization of solutions of polycarbazolyldiacetylene PolyDCHD-HS at 1064 and 1500 nm by Z-scan, Laser Physics**12**, 2002, p. 707.
[23] S. Santran, L. Canioni, L. Sarger, T. Cardinal, E. Fargin, Precise and absolute measurements of the complex third-order optical susceptibility, J. Opt. Soc. Am. B 21 (12) (2004) 2180–2190.
[24] P.W. Smith, W.J. Tomlinson, D.J. Eilenberger, P.J. Maloney, Measurement of electronic optical Kerr coefficients, Opt. Lett. 6 (12) (1981) 581–583.
[25] T. Töpfer, J. Hein, J. Philipps, D. Ehrt, R. Sauerbrey, Tailoring the nonlinear refractive index of fluoride-phosphate glasses for laser applications, Appl. Phys. B 71 (2000) 203–206.

[26] B. Momgaudis, S. Guizard, A. Bilde, A. Melninkaitis, Nonlinear refractive index measurements using time-resolved digital holography, Optic Lett. 43 (2018) 304.
[27] G.A. Slack, Phys. Rev. 112 (5) (1961) 1451–1464.
[28] S. Normani, A. Braud, J.L. Doualan, R. Moncorgé, C. Maunier, D. Stoffel, P. Camy, Nd^{3+} and Lu^{3+} Doped CaF$_2$ Crystals as Novel Amplifier Materials for High-Energy Infrared Lasers, in: International Conference on Transparent Optical Networks, ICTON), Trento, 2016, pp. 1–4, https://doi.org/10.1109/ICTON.2016.7550654.
[29] M. De Vido, D. Meissner, S. Meissner, K. Ertel, P.J. Phillips, P.D. Mason, S. Banerjee, T.J. Butcher, J.M. Smith, C. Edwards, C. Hernandez-Gomez, J. L. Collier, Characterisation of adhesive-free bonded crystalline Yb:YAG for high energy laser applications, Opt. Mater. Express 7 (2017) 425.
[30] O. Morice, Miro: complete modeling and software for pulse amplification and propagation in high-power laser systems, Opt. Eng. 42 (2003) 1530.
[31] D.J. Kane, R. Trebino, Characterization of arbitrary femtosecond pulses using frequency-resolved optical gating, IEEE J. Quant. Electron. 29 (2) (1993) 571–579.
[32] R. Adair, L.L. Chase, S.A. abd Payne, Nonlinear refractive index of optical crystals, Phys. Rev. B 39 (5) (1989) 3337.

[33] G.B. Altshuler, A.I. Barbashev, V.B. Karasev, K.I. Krylov, V.M. Ovchinnikov, &S. F. Sharlai, Direct measurement of the tensor elements of the nonlinear optical susceptibility of optical materials, Pisma v Zhurnal Tekhnischeskoi Fiziki 3 (1977) 523–528.
[34] D. Milam, M.J. Weber, Measurement of nonlinear refractive-index coefficients using time-resolved interferometry: application to optical materials for high-power neodymium lasers, J. Appl. Phys. 47 (6) (1976) 2497–2501.
[35] W.L. Smith, J.H. Bechtel, N. Bloembergen, Dielectric-breakdown threshold and nonlinear-refractive-index measurements with picosecond laser pulses, Phys. Rev. B 12 (2) (1975) 706.
[36] R. De Salvo, A.A. Said, D.J. Hagan, E.W. Van Stryland, M. Sheik-Bahae, Infrared to ultraviolet measurements of two-photon absorption and n$_2$ in wide bandgap solids, IEEE J. Quant. Electron. 32 (8) (1996) 1324–1333.
[37] D. Milam, Review and assessment of measured values of the nonlinear refractive-index coefficient of fused silica, Appl. Optic. 37 (3) (1998) 546–550.
[38] R. Adair, L.L. Chase, A. Payne, Dispersion of the nonlinear refractive index of optical crystals, Opt. Mater. 1 (3) (1992) 185–194.